

Cite this: *Dalton Trans.*, 2025, **54**, 6623

# Quantum chemical elucidation of the luminescence mechanism in a europium(III) co-doped UiO-66 chemosensor selective to mercury(II)<sup>†</sup>

Yoan Hidalgo-Rosa,<sup>1</sup> Yoslainy Echevarria-Valdés,<sup>2</sup> Mario Saavedra-Torres,<sup>3</sup> Dayán Páez-Hernández,<sup>4</sup> Eduardo Schott<sup>5</sup>\*<sup>f</sup> and Ximena Zarate<sup>6</sup>\*<sup>d</sup>

Lanthanide(III) ions can be incorporated into metal–organic frameworks (MOFs) to form Ln@MOFs through post-synthetic procedures. This makes the MOFs efficient luminescent chemical sensors for detecting trace amounts of heavy metals. In this report, a quantum chemical theoretical protocol has been carried out to elucidate the detection principle of the turn-off luminescence mechanism in a Eu@UiO-66(DPA)-type MOF selective to Hg<sup>2+</sup> ions. UiO-66(DPA) is an iso-reticular MOF of UiO-66 constructed from the Zr<sub>6</sub>-cluster [Zr<sub>6</sub>(μ<sub>3</sub>-O)<sub>4</sub>(μ<sub>3</sub>-OH)<sub>4</sub>]<sup>12+</sup> and the ligands 1,4-benzenedicarboxylate (BDC) and 2,6-pyridinedicarboxylate (DPA) as linkers. The sensitization and energy transfer (ET) in UiO-66(DPA) doped with Eu<sup>3+</sup> were analyzed using multireference *ab initio* CASSCF/NEVPT2 methods and time-dependent density functional theory (TD-DFT). The cluster model used in the calculations comprises the Z<sub>6</sub>-cluster/BDC/DPA fragments with the DPA ligand coordinating to Eu<sup>3+</sup> or Hg<sup>2+</sup> ions. The proposed sensitization pathway involves intersystem crossing from S<sub>1</sub>(DPA) to T<sub>1</sub>(DPA), a plausible subsequent energy transfer from T<sub>1</sub>(DPA) to the <sup>5</sup>D<sub>1</sub> state of Eu<sup>3+</sup>, and then vibrational relaxation to the emissive <sup>5</sup>D<sub>0</sub> state. These results also suggest that the electronic states of the BDC ligand can be strengthened by the population of the T<sub>1</sub> electronic states of the DPA antenna *via* ET. Periodic DFT calculations confirm the electronic state mixture of BDC and DPA linkers in the conduction bands, just above the electronic state of Eu<sup>3+</sup> ions, which is in concordance with the proposed Eu<sup>3+</sup> sensitization pathways. The assessed optical properties (absorption and emission) of Hg<sup>2+</sup>@UiO-66(DPA) explain the experimental behavior of this chemosensor when the Hg<sup>2+</sup> ion replaces the Eu<sup>3+</sup> ion and the luminescence diminishes.

Received 24th November 2024,  
Accepted 13th March 2025

DOI: 10.1039/d4dt03285c

rsc.li/dalton

<sup>a</sup>Centro de Nanotecnología Aplicada, Facultad de Ciencias, Ingeniería y Tecnología, Universidad Mayor, Camino La Pirámide 5750, Huechuraba, Santiago, Chile.

E-mail: yoanhrj@gmail.com

<sup>b</sup>Escuela de Ingeniería del Medio Ambiente y Sustentabilidad, Facultad de Ciencias, Ingeniería y Tecnología, Universidad Mayor, Camino La Pirámide 5750, Huechuraba, 8580745 Santiago, Chile<sup>c</sup>Doctorado en Fisicoquímica Molecular, Facultad de Ciencias Exactas, Universidad Andrés Bello, República 275, Santiago 8370146, Chile<sup>d</sup>Instituto de Ciencias Aplicadas, Facultad de Ingeniería, Universidad Autónoma de Chile, Av. Pedro de Valdivia 425, Santiago, Chile.

E-mail: ximena.zarate@uautonoma.cl

<sup>e</sup>Center of Applied Nanosciences (CANS), Universidad Andres Bello, Ave. República #275, 8370146 Santiago de Chile, Chile<sup>f</sup>Departamento de Química Inorgánica, Facultad de Química y de Farmacia, Centro de Energía UC, Centro de Investigación en Nanotecnología y Materiales Avanzados CIEN-UC, Pontificia Universidad Católica de Chile, Vicuña Mackenna 4860, Macul, 7820436 Santiago, Chile. E-mail: maschotte@gmail.com, edschott@uc.cl<sup>†</sup>Electronic supplementary information (ESI) available. See DOI: <https://doi.org/10.1039/d4dt03285c>

## Introduction

In recent years, the use of chemical methods for detecting metal ions has gained considerable importance.<sup>1</sup> This shift is driven by growing concerns over environmental pollution and the health risks posed by metal ion contamination.<sup>2,3</sup> Chemical detection methods play a crucial role in monitoring and controlling the metal ion levels in various settings, including water sources, food products, and industrial processes.<sup>3</sup> Chemical detection relies on chemical transformation or a change in the physical property induced by specific interactions between target analytes (such as metal ions, small molecules, biomarkers, and others) and the chemosensor.<sup>4</sup> Optical chemosensors have gained significant attention in the development of selective and efficient tools for metal ion detection, due to their ability to provide instantaneous data regarding a particular analyte. Many ions (like Mg<sup>2+</sup>, Ca<sup>2+</sup>, K<sup>+</sup>, F<sup>-</sup>, etc.) are essential in biological systems and play a crucial role in different biochemical processes.<sup>3</sup> For example, fluoride



is one type of valuable trace element of the human body; nevertheless, excessive fluoride in the organism causes serious health issues such as dental and skeletal fluorosis. Metal ions constitute biological electrolytes that must be controlled for people on Earth and also for astronauts in space. At certain concentrations, other metals such as copper (Cu), chromium and zinc are necessary for the suitable function of the human body. However, when the homeostatic concentration of these metal ions is exceeded, they turn into a poison. In contrast, lead, cadmium and mercury (Hg), even at trace concentrations, cause irreversible alterations in the health of living beings. So, for the protection of human health, not only the knowledge of their effects but also their detection and monitoring is necessary.<sup>5,6</sup>

Optical sensors can be based on various principles, including absorbance, transmittance, polarization of light or refractive index.<sup>7</sup> Advances in chemical detection technologies have allowed for more sensitive and selective detection of metal ions, even at trace levels.<sup>8</sup> This has enabled researchers and environmental agencies to better understand metal ion distribution, sources, and potential health risks. Furthermore, developing portable chemical detection devices has significantly enhanced on-site monitoring and rapid screening of metal ion contamination.<sup>9</sup> In 2020, Yuxiu Xiao *et al.* reported an analytical device based on a one-to-two logic gate utilizing a Eu-MOF. They designed a Eu-MOF-loaded fiber paper micro-sensor for the rapid detection of water in solid pharmaceuticals using ratiometric sensing and a portable visual device.<sup>10</sup> Building on this advancement, the integration of metal-organic frameworks (MOFs) with smartphone technology has further unlocked new possibilities for real-time, on-site chemical detection.<sup>11–13</sup> Lanthanide-based MOFs (Ln-MOFs) have shown exceptional promise for visual detection applications through smartphone-assisted systems,<sup>13–15</sup> leveraging their distinctive luminescence properties to enhance sensitivity and enable accurate quantification *via* straightforward and interpretable colorimetric or luminescence changes.<sup>11,14</sup>

In this regard, luminescent metal-organic frameworks (L-MOFs) are promising alternatives in the development of chemosensors.<sup>16</sup> These materials are composed of metal ions or clusters (nodes) connected by organic ligands (linkers), generating two-dimensional or three-dimensional structures.<sup>17</sup> The combination of these metallic and organic building components (nodes and linkers) in L-MOFs leads to the appearance of unique luminescence properties. The hybrid nature of their components enables a wide range of photophysical processes that govern their luminescence properties.<sup>18</sup> Metal-to-ligand charge transfer (MLCT), ligand-to-metal charge transfer (LMCT), ligand-to-ligand charge transfer (LLCT), metal localized emission and ligand-centered emission are some of the involved mechanisms.<sup>19</sup> These materials exhibit luminescence changes in the presence of specific analytes, allowing the detection and recognition of target substances.<sup>20</sup> Other features of MOFs that make them stand out as optical chemosensors are related to their tunable structures, high surface areas, and easy functionalization post-synthesis.<sup>21,22</sup> These properties make L-MOFs highly useful in fields such as

environmental monitoring,<sup>23</sup> biomedical research,<sup>24</sup> and industrial applications.<sup>25</sup> Therefore, by understanding and tuning the luminescence changes in L-MOFs, researchers would be able to design highly sensitive and selective chemosensors for a wide range of analytes.<sup>26</sup>

In this sense, linkers can be designed or functionalized by post-synthetic modifications (PSM) to exhibit specific properties, such as desirable optical properties, and/or induce certain chemosensor-analyte interactions.<sup>27</sup> A powerful PSM strategy is to include lanthanide ions (Ln<sup>3+</sup>) into MOF hosts to activate the emission properties of the material and generate new emission signals that are lanthanide ion-centered.<sup>28</sup> The sharp line emissions, high color purity, high luminescence quantum yield, and large Stokes shifts, attributed to the 4f–4f transitions and relativistic effects of Ln ions, might undergo improvements in co-doped MOFs.<sup>29</sup> Their luminescence arises from a sensitization process carried out *via* energy transfer (ET) from a suitable organic ligand to the Ln<sup>3+</sup> ions, which is called the “antenna effect”. Thus, a careful selection and design of the linkers and nodes might tune the emission properties of L-MOFs. This makes L-MOFs promising materials for the development of efficient and sensitive chemosensors.<sup>30–32</sup> Due to their structural and optical properties, L-MOFs functionalized with Ln<sup>3+</sup> ions have been used to detect metal ions.<sup>33,34</sup> Mechanisms such as energy transfer from the ligand to the Ln<sup>3+</sup> center and metal–ligand charge transfer are well accepted in a detection process to explain the change in the optical properties of functionalized L-MOFs.<sup>34,35</sup> Several studies indicate that the quenching effect is not completely clear in all cases. In this context, a recent systematic literature review by Shuangyan Wu (2024)<sup>36</sup> concluded that the principles underlying the current sensing mechanisms are unclear and limited to qualitative analysis. However, much research has been descriptive and based only on experimental data. Some works have successfully applied DFT-based methods to elucidate potential photophysical processes that induce luminescence alteration in Ln<sup>3+</sup> co-doped L-MOFs.<sup>37–39</sup> However, in Ln<sup>3+</sup>-based systems, a more sophisticated level of theory is required to accurately address the multireference character arising from the various low-lying states associated with the 4f<sup>*n*</sup> configurations.<sup>40</sup> Predicting the correlation between the L-MOF structure and analyte-induced luminescence changes is challenging due to the large size of MOFs. However, advancements in computational chemistry have enabled accurate descriptions of their molecular and electronic properties.<sup>26,41–46</sup> This report presents a computational protocol designed to understand the luminescence properties and sensing mechanisms of Ln<sup>3+</sup> co-doped L-MOFs (Ln<sup>3+</sup>@L-MOFs). A comprehensive study was conducted, focusing on molecular and electronic properties, including the relative energies of the ground and excited states (S<sub>1</sub> or T<sub>1</sub>), as well as the electronic band structures of the L-MOFs. Our theoretical protocol integrates periodic DFT, molecular DFT, and multireference calculations to provide a detailed assessment of the luminescence properties and sensing mechanism.<sup>26,43–45</sup>



Theoretical studies of  $\text{Ln}^{3+}@L\text{-MOF}$  chemosensors, due to their computational complexity, numerous electrons and electron correlation effects, need high-performance computation resources. These studies are crucial in the investigation of  $\text{Ln}^{3+}@L\text{-MOFs}$ , offering in-depth knowledge of the principles underlying detection events toward a target analyte, thereby influencing experimental work and aiding in creating new chemosensors of the  $\text{Ln}^{3+}@L\text{-MOF}$  type.

Hence, to enhance the understanding and contribute to the knowledge, in the work reported herein, a theoretical procedure is proposed. In this theoretical procedure, multiconfigurational *ab initio* methods, along with molecular density functional theory (DFT), and periodic DFT calculations were combined. This approach aims to accurately determine the sensitization and emission channels for the previously experimentally reported UiO-66 MOFs<sup>47</sup> doped with a  $\text{Eu}^{3+}$  selective chemical sensor to detect  $\text{Hg}^{2+}$  *in situ* as well as, to the best of our knowledge, the sensing mechanism for the first time.

This MOF holds the  $\text{Eu}^{3+}$  atom in a free  $-\text{COOH}$  group ( $\text{Eu}@UiO\text{-}66(\text{DPA})$ ) and it is used to detect very low  $\text{Hg}^{2+}$  levels (lower than 10 nM, which is the maximum level of  $\text{Hg}^{2+}$  in drinking water according to the U.S. Environmental Protection Agency<sup>48</sup>). It is proposed that the detection mechanism is *via* the replacement of the  $\text{Eu}^{3+}$  atom by the  $\text{Hg}^{2+}$  atom due to the higher affinity of DPA toward  $\text{Hg}^{2+}$ . This substitution induces the blocking of the  $\text{Eu}^{3+}$  antenna effect inducing then the chelation enhancement quenching (CHEQ) effect (Fig. 1).

## Computational methods

Quantum chemistry offers reliable tools for gaining a deep understanding of the sensing mechanisms in co-doped MOFs. A careful examination of the detection principles is essential for designing new luminescent MOF-based chemosensors and facilitating their transition from experimental research to developing MOF-based portable devices.<sup>49</sup> Consequently, rigorous investigations are still required to achieve a more rational design of  $\text{Ln}^{3+}@L\text{-MOF}$  chemosensors.

One of the most intriguing features of MOFs is their ability to fine-tune optical properties through slight structural modifi-

cations. These modifications can include the incorporation of functional groups<sup>50</sup> or metal ions<sup>51</sup> or be induced by the analyte,<sup>52</sup> which involved a significant change in the optical properties of MOFs. The photophysical processes that dictate the optical behaviors of a luminescent sensor are intrinsically associated with electronic interactions between the sensor and the analyte.<sup>53</sup> The density of states (DOS) method has been widely utilized to investigate the electronic structure and optical properties of MOF-based chemical sensors.<sup>52–57</sup> DOS plots provide crucial insights into the nature of charge transport, helping to determine whether it occurs through ligand-to-ligand, metal-to-ligand, ligand-to-metal, or metal-to-metal processes involving the photophysical properties of materials.<sup>41,58</sup> This analysis offers a straightforward approach for representing complex electronic structures while also providing valuable insights into the optical properties of materials.<sup>59</sup> This method has been previously employed to gain insights into the photophysical processes associated with optical properties related to charge transfer and energy transfer mechanisms,<sup>60</sup> such as ligand–ligand charge transfer (LLCT),<sup>61</sup> metal-to-ligand charge transfer (MLCT),<sup>57</sup> ligand-to-metal charge transfer (LMCT),<sup>62</sup> and photoinduced electron transfer (PET).<sup>57</sup> Additionally, it provides a detailed view of the atomic contributions to the occupied and unoccupied electronic states.<sup>60,61,63,64</sup> Thus, DOS analysis was employed to further investigate the changes in the luminescence properties of the UiO-66(DPA) chemosensor induced by  $\text{Eu}^{3+}$  and  $\text{Hg}^{2+}$  ions, focusing on the structures  $\text{Eu}@UiO\text{-}66(\text{DPA})$  and  $\text{Hg}@UiO\text{-}66(\text{DPA})$ .

On the other hand, to study the efficiency of Ln sensitization and emission in a MOF, the main processes involved must be considered. This process starts from the excitation of the linker with the final population of its first excited singlet state ( $S_1$ ) after no radiative processes followed by an intersystem crossing (ISC) between  $S_1$  and the first excited triplet state ( $T_1$ ) of the linker [linker ( $S_1 \rightarrow T_1$ )]. Finally, there occurs an energy transfer process that populates the emissive state of the lanthanide ion [linker ( $T_1 \rightarrow \text{Ln}^{3+}$ )] from which emission occurs.<sup>26</sup>

Thus, to elucidate the origin of the sensitization and emission pathways and the sensing mechanism in  $\text{Ln}^{3+}@L\text{-MOF}$  chemosensors, a detailed understanding of the electronic structure of the system and the effect of the presence of the

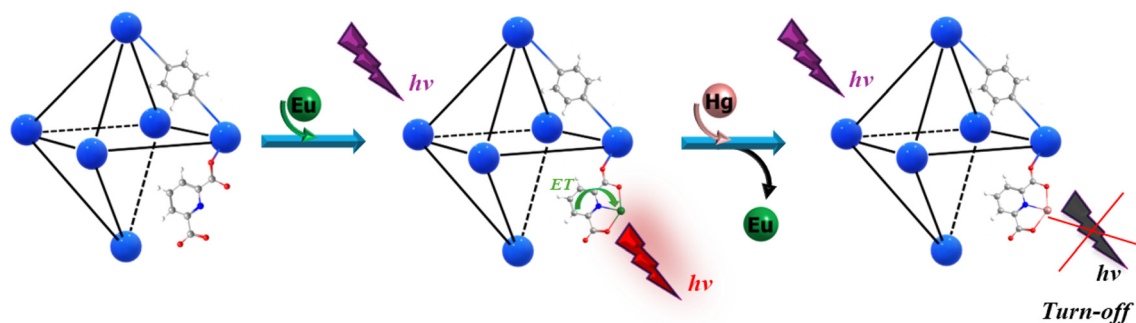


**Fig. 1** A simplified scheme showing the detection mechanism *via* the replacement of  $\text{Eu}^{3+}$  by  $\text{Hg}^{2+}$ , inducing the blocking of the antenna effect of  $\text{Eu}^{3+}$  and then producing the CHEQ effect.



analyte of interest must be obtained. This implies predicting the correct localization of the electronic state of the lanthanide ions and antenna both in the ground state and excited states.<sup>40</sup> Advanced computational methods have been developed that enable a more in-depth examination of the electronic structure and excited states related to photophysical processes that govern luminescence properties.

Due to the intrinsic properties of heavy elements, such as lanthanides, their theoretical treatment requires meticulous evaluation.<sup>26,65</sup> Three primary factors must be considered: (i) relativistic effects, including scalar relativistic contributions and spin-orbit coupling, (ii) electronic correlation, and (iii) the influence of the ligand field.<sup>66</sup> In the case of lanthanides, spin-orbit interactions and electron correlation effects play a dominant role and must be explicitly accounted for in theoretical calculations. Notably, the quasi-degenerate nature of electronic configurations arising from the  $4f^n$  shell introduces significant static correlation, which is essential for accurately determining the energetic positions of both ground and excited states.<sup>40,67</sup>

One of the most important methods is the multi-configuration self-consistent field (MCSCF), which is employed to study the electronic structure of lanthanide ions.<sup>68</sup> Therefore, our attention has been directed towards accomplishing a theoretical protocol to clarify the emission channels and understand the sensing mechanism in luminescent UiO-66 (DPA) sensors using a cluster model. In the ESI,† we present a detailed description of structural models used for modeling these systems, both as extended solids and cluster models. Moreover, the computational methods are described in detail, such as software packages, theory levels, and theoretical approaches used for each of the calculations.

## Results and discussion

### Periodic modelling of $\text{Eu}^{3+}@\text{UiO-66}(\text{DPA})$ and $\text{Hg}^{2+}@\text{UiO-66}(\text{DPA})$

Cell parameters were optimized, compared with the experimental crystal data,<sup>47</sup> and modified in agreement with the

herein studied models, *i.e.* to obtain periodic models of  $\text{Eu}^{3+}@\text{UiO-66}(\text{DPA})$  and  $\text{Hg}^{2+}@\text{UiO-66}(\text{DPA})$  shown in Fig. S1.† The obtained structures were finally reoptimized.

For UiO-66(Zr) MOFs, it has been documented that their optical properties are governed by electronic transitions involving both non-functionalized BDC linkers and substituted BDC linkers. Matsuoka *et al.*<sup>69</sup> demonstrated that the organic linker in  $\text{NH}_2\text{-UiO-66}(\text{Zr})$  absorbs light, as shown by *in situ* electron paramagnetic resonance (EPR) measurements conducted before and after exposure to visible light. The EPR measurements revealed no characteristic signals attributable to  $\text{Zr}^{3+}$  species after visible-light exposure, indicating that LMCT does not occur in this system. Jorge Gascon *et al.* reached a similar conclusion while investigating the electronic properties of  $\text{NH}_2\text{-UiO-66}(\text{Zr})$  and  $\text{NH}_2\text{-UiO-66}(\text{Hf})$  MOFs using DFT and EPR techniques. They emphasized that there is no evidence for the formation of  $\text{M}^{3+}$  species, such as  $\text{Zr}^{3+}$  or  $\text{Hf}^{3+}$  in the excited state.<sup>70</sup> On the other hand, previous theoretical studies reported the electronic structure of the UiO-66(Zr), UiO-66(Hf) and UiO-(Th) MOFs *via* density of states (DOS) and projected DOS (PDOS) plots. In these previous studies, the contributions of ligand states near the conduction band minimum (CBM) and valence band maximum (VBM) were also shown.<sup>62,71</sup> Accordingly, to gain deeper insights into the emission pathway of the sensing mechanism, the PDOSs of both the  $\text{Eu}^{3+}@\text{UiO-66}(\text{DPA})$  and  $\text{Hg}^{2+}@\text{UiO-66}(\text{DPA})$  systems were analyzed.

PDOS analysis by fragments is shown in Fig. 2. BDC fragments are predominantly present in the occupied range, particularly in the valence zone with higher contribution states between  $-7$  and  $-1.8$  eV (purple), while DPA (blue) and  $\text{Zr}_6\text{O}_4(\text{OH})_4$  (red) are also present but with a small number of states. However, the Eu state emerged with a lone but highly populated band closer to the Fermi level at  $-0.1$  eV. The lowest energy conduction band is populated almost entirely by Eu states (green curve) at  $1.1$  eV, and only with small contributions by the DPA linker at this energy level. Thus, doping UiO-66(DPA) with  $\text{Eu}^{3+}$  introduces  $4f$  states that are sufficiently

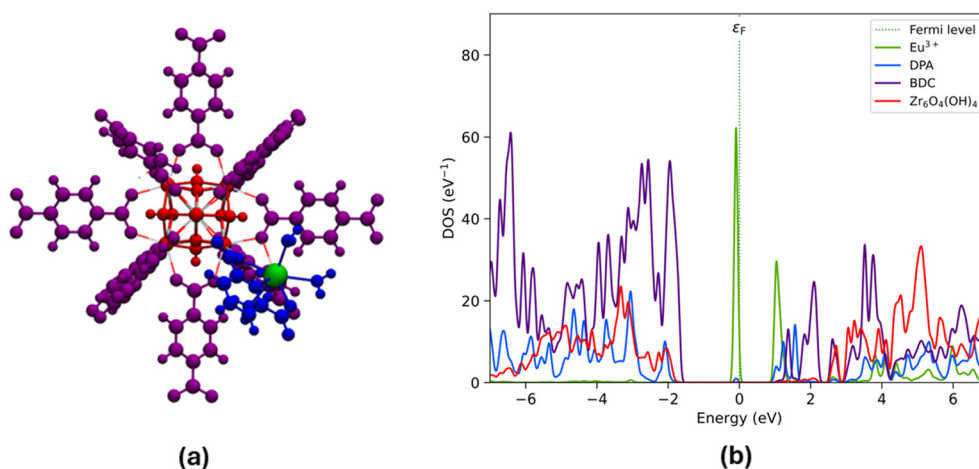


Fig. 2 (a) Structure of  $\text{Eu}^{3+}@\text{UiO-66}(\text{DPA})$  identifying fragments:  $\text{Zr}_6\text{O}_4(\text{OH})_4$  (red), BDC (violet), DPA (blue), and Eu (green). (b) PDOS by fragments.



low in energy to fall below the electronic states of the BDC and DPA linkers. The rest of the fragments contribute above  $\sim 1.1$  eV, mainly DPA (between 1.1 and 2.2 eV) and BDC (mostly between 1.5 and 2 eV). The overlap between the electronic states of the DPA and BDC linkers next to  $\text{Eu}^{3+}$  (1.5 to 2.2 eV) suggests that both ligands are involved in the sensitization and emission pathways of the  $\text{Eu}^{3+}@UiO-66(\text{DPA})$  MOF.

PDOS results obtained by elemental and orbital analyses presented in Fig. 3 are in agreement with the by-fragment results. It is observed that the valence band located closer to the Fermi level is populated mainly by Eu(f), followed by O(p) and C(p) between  $-2$  and  $-7$  eV, assigned previously to the BDC and  $\text{Zr}_6\text{O}_4(\text{OH})_4$  fragments. However, O(p) mostly contributes at lower energy levels under  $-2$  eV, attributed to the O atoms present on the  $\text{Zr}_6\text{O}_4(\text{OH})_4$  and BDC/DPA terminal groups. The conduction band is also populated by Eu(f) at 1

eV, followed by C(p) from BDC and DPA, particularly between 1 and 2.2 eV. Over this range,  $\text{Zr}_6\text{O}_4(\text{OH})_4$  shows an increase in the number of unoccupied states, through Zr(d), with Eu(d) and the rest of the elements showing values over 4 eV.

$\text{Eu}^{3+}@UiO-66(\text{DPA})$  exhibits alterations in the luminescence intensity after the introduction of various ions, with a particularly pronounced effect observed in the presence of  $\text{Hg}^{2+}$  ions. Experimental data suggest that the quenching mechanism may involve the substitution of  $\text{Eu}^{3+}$  by  $\text{Hg}^{2+}$  within the  $\text{Eu}^{3+}@UiO-66(\text{DPA})$  structure. This substitution leads to a reduction in the material luminescence.<sup>47</sup> To get a deeper understanding of the sensing mechanism, PDOS analysis of  $\text{Hg}^{2+}@UiO-66(\text{DPA})$  was also performed.

PDOS by-fragment results (Fig. 4) show that at the Fermi level, the BDC fragments would have a relevant role with their occupied states in the valence zone around  $-2.0$  eV (purple).

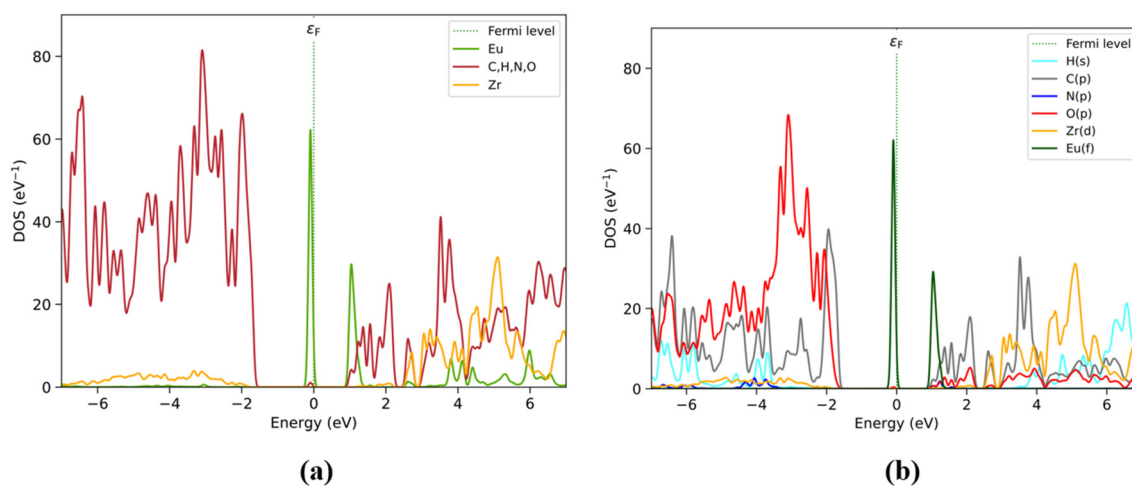


**Fig. 3** PDOS by elements (with organic elements C, H, N, and O as a single group) (a) and shells (b) considering those most relevant to  $\text{Eu}^{3+}@UiO-66(\text{DPA})$ . Color labels for (a): Eu (green), organic group (red) and Zr (orange). For (b): H(s) (cyan), C(p) (grey), N(p) (blue), O(p) (red), Zr(d) (orange), and Eu(f) (dark green).

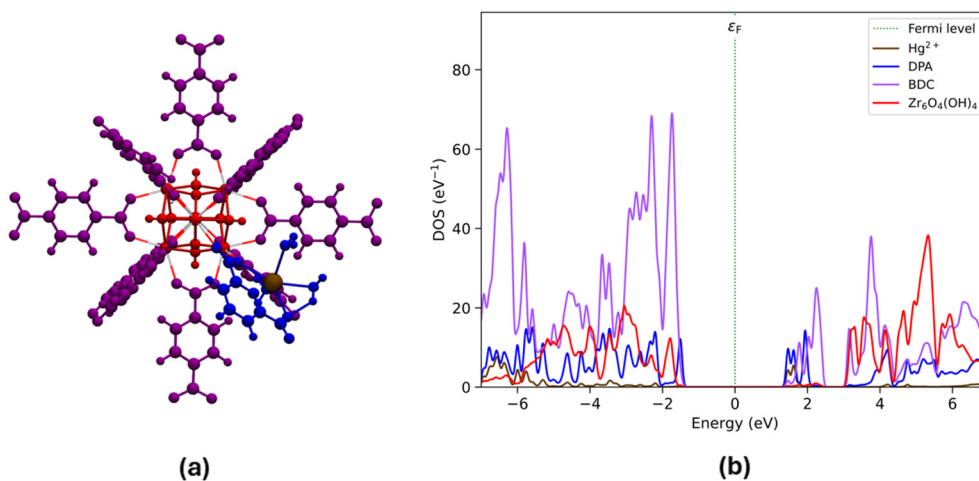


**Fig. 4** (a) Structure of  $\text{Hg}^{2+}@UiO-66(\text{DPA})$  identifying fragments:  $\text{Zr}_6\text{O}_4(\text{OH})_4$  (red), BDC (violet), DPA (blue), and Hg (brown). (b) PDOS by fragments.



Also, DPA (blue) is the fragment that maintains direct interactions with the Hg atom and this atom does not show a relevant contribution in this region. The BDC fragment also shows some contributions at around  $-1.8$  and  $-2.5$  eV, sharing the same energy range with the  $Zr_6O_4(OH)_4$  and DPA fragments. However, the  $Zr_6O_4(OH)_4$  and DPA fragments show much smaller contributions than BDC. On the other hand, at low energy levels, the conduction band is composed of a Hg atom ( $1.5$  eV) and followed by the DPA fragment. Around this range, the DPA and BDC fragments maintain a relevant contribution up to  $2.5$  eV, especially the BDC fragment shows an important contribution between  $1.8$  and  $2.5$  eV. Over  $3$  eV, the  $Zr_6O_4(OH)_4$  and BDC fragments share their contributions to the PDOS, followed by the contribution of the DPA fragment with an overlap at larger energy values.

The PDOS obtained by elemental and shell analyses matches these results (Fig. 5), where the valence band is composed mainly of C(p) followed by O(p) at  $-2$  eV. The O(p) contribution increases at lower energy levels assigned to the  $Zr_6O_4(OH)_4$  and BDC/DPA fragments. On the other hand, the conduction band is composed of C(p) and Hg(s) orbitals at  $\sim 1.8$  eV. Moreover, C(p) and O(p) unoccupied state contributions are present between the  $1.8$  and  $2.5$  eV energy range. Finally, over the  $3$  eV energy range, Zr(d) and H(s) contribute to those states.

The electronic states introduced by the Hg atoms and the DPA linkers generate unoccupied states at the conduction band edge, leading to the formation of a non-emissive excited state. According to our analysis, the  $Hg^{2+}$  and DPA composition of the conduction band edge in the  $Hg^{2+}@UiO-66(DPA)$  system contributes to generate a 'dark' excited state after excitation and subsequent non-radiative deactivation. This 'dark' excited state leads to a turn-off in the luminescence process. This result is consistent with the experimental turn-off luminescence sensing mechanism of  $Eu^{3+}@UiO-66(DPA)$  in the presence of  $Hg^{2+}$  ions.

Finally, for  $Eu^{3+}@UiO-66(DPA)$  and  $Hg^{2+}@UiO-66(DPA)$ , the highest occupied levels are constituted by  $Eu^{3+}$  and DPA/BDC linkers, respectively. In particular, for  $Hg^{2+}@UiO-66(DPA)$ , the C(p) orbitals have an important contribution, *i.e.* the phenyl groups. On the other hand, both metals contribute primarily at low energy unoccupied levels of the conduction band. Specifically, the most notable orbital contribution of Eu has an energy of  $1.1$  eV, while for  $Hg^{2+}@UiO-66(DPA)$ , the same region of the conduction band is composed of Hg and DPA states (Fig. 4b). This difference in composition would lead to expected energy transfer channels from the BDC fragments to the metals ( $Eu^{3+}$  or  $Hg^{2+}$ ) and the DPA fragment. This charge transfer is particularly more favorable in the case of  $Eu^{2+}@UiO-66(DPA)$  than in the case of  $Hg^{2+}@UiO-66(DPA)$ , which could be explained by the lower band gap in the electronic structure of the material with the lanthanide.

### Periodic modelling of $Eu^{3+}Hg^{2+}@UiO-66(DPA)$

In a supercell model containing both  $Hg^{2+}$  and  $Eu^{3+}$  ions, the DPA linker was considered to possess vacant coordination sites, with the free  $-COOH$  groups and pyridine nitrogen atoms acting as coordination sites for metal ions. This theoretical investigation aligns with the experimentally proposed mechanism, which attributes the luminescence quenching to the substitution of  $Eu^{3+}$  ions by  $Hg^{2+}$  ions. According to Fig. S2,† and for this specific model where both ligands occupy the same site on each node, the metal-metal (Eu–Hg) distance is  $14.68$  Å. This value is close to the distance between replicas of two equivalent BDC linkers, which is  $14.65$  Å. This large separation between the metal centers suggests that any form of energy transfer (ET) between them is negligible, as there is no intervening electronic spacer to facilitate such a process. It is important to note that the energy transfer (ET) rates depend significantly on the donor–acceptor (D–A) separation distance ( $R$ ) and the mechanism involved. For Förster resonance energy transfer (FRET), the ET rate decreases with

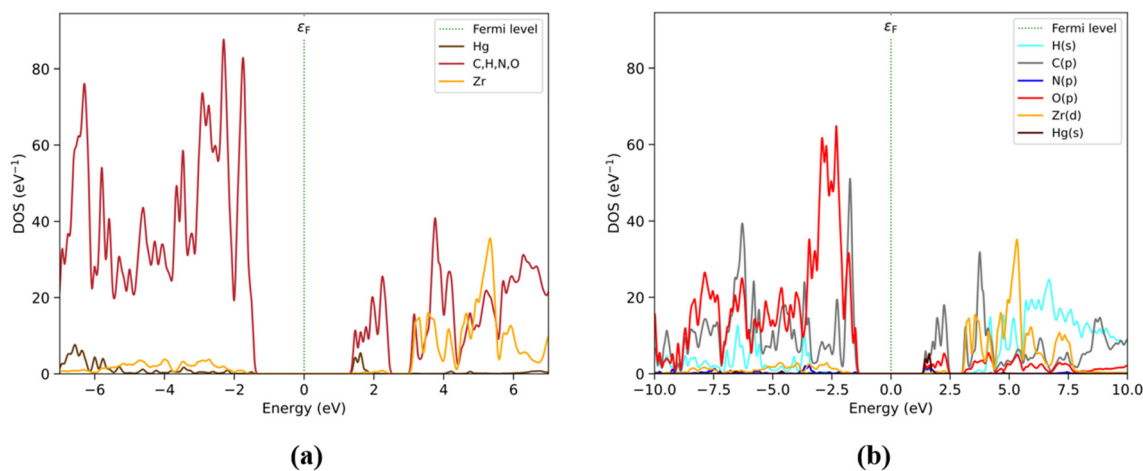


Fig. 5 PDOS by elements (with organic elements C, H, N, and O as a single group) (a) and shells (b) considering those most relevant to  $Hg^{2+}@UiO-66(DPA)$ . Color labels for (a): Hg (brown), organic group (red) and Zr (orange). For (b): H(s) (cyan), C(p) (grey), N(p) (blue), O(p) (red), Zr(d) (orange), and Hg(s) (brown).



increasing  $R$ , following an inverse sixth power relationship ( $1/R^6$ ). In contrast, the Dexter energy transfer mechanism exhibits an ET rate that decays exponentially with increasing D–A distance due to its dependence on wavefunction overlap. We concur with the mechanism proposed in the experimental work,<sup>47</sup> which suggests that the substitution of  $\text{Eu}^{3+}$  ions by  $\text{Hg}^{2+}$  ions within the structure reduces the number of emission centers, thereby diminishing the material's luminescence as the  $\text{Hg}^{2+}$  ion concentration increases. Given that the mechanism is well supported by experimental evidence, our study focuses on characterizing and quantifying the luminescence response rather than investigating the substitution process in detail with a model involving both ions. This approach allows us to align our efforts with the primary goal of elucidating the emission mechanisms of  $\text{Eu}^{3+}@ \text{UiO}(\text{DPA})$  and non-emissive states induced by the inclusion of  $\text{Hg}^{2+}$ . Inspired by these results, the sensitization and emission of the  $\text{Eu}^{3+}$ -doped  $\text{UiO-66}(\text{DPA})$  MOF and the role of  $\text{Hg}^{2+}$  in the turn-off luminescence mechanism were investigated. To achieve this, accurate multiconfigurational *ab initio* methods were used along with DFT calculations using cluster models; see Fig. S3(a) and (b).† The next section provides a more insightful understanding of the luminescence properties of  $\text{Eu}^{3+}@ \text{UiO-66}(\text{DPA})$  and its selective quenching response to  $\text{Hg}^{2+}$  ions.

### Optical properties of $\text{Eu}^{3+}@ \text{UiO-66}(\text{DPA})$

The simulated UV–Vis absorption spectrum of  $\text{Eu}^{3+}@ \text{UiO-66}(\text{DPA})$  displays two main vertical transitions based on the strength of the oscillator ( $f$ ), which are very close in energy. The first one (labelled as A) appears centered at around 272 nm ( $f = 0.970$ ), which corresponds to  $\pi \rightarrow \pi^*$  electronic transition. Table S1† shows that the electron density of the molecular orbitals involved in this electronic transition is located on the BDC linker. The second absorption band located at 278 nm ( $f = 0.175$ ) is also assigned to linker-centered  $\pi \rightarrow \pi^*$  electronic transition and involves the active molecular orbitals of the DPA linkers. This result shows a difference of about 50 nm compared to the experimental value (305 nm),<sup>22</sup> which falls within the usual error margin accepted for TD-DFT calculations. Based on this result, it is possible to apply the fragmentation scheme developed by Beltrán-Leiva *et al.*<sup>40</sup> to evaluate the most likely sensitization and emission pathways in lanthanide complexes. In this approach, the ligand and the lanthanide fragments are calculated separately (at the same level of theory), using multiconfigurational methods. The author points out that it is crucial to consider that absorption is ligand-localized. This guarantees that excitation bands involved in the sensitization channel are not affected by the fragmentation procedure. Based on this approach, a definitive understanding of the possible sensitization and emission pathways of  $\text{Eu}^{3+}@ \text{UiO-66}(\text{DPA})$  systems is provided in the next section.

### Sensitization and emission pathways of $\text{Eu}^{3+}@ \text{UiO-66}(\text{DPA})$

The sensitization pathway and emission mechanisms of the  $\text{Eu}^{3+}@ \text{UiO-66}(\text{DPA})$  system were studied through a multirefer-

ence CASSCF/NEVPT2 approach. The ground states and excited electronic states of the  $\text{Eu}^{3+}$  fragment were explored *via* CAS(6,7)SCF/NEVPT2 calculations. At the theoretical level the calculations show that the emitting level ( $^5\text{D}_0$ ) state and  $^5\text{D}_1$  of  $\text{Eu}^{3+}$  are located at 17 600  $\text{cm}^{-1}$  and 20 174  $\text{cm}^{-1}$ , respectively. Our results align with previous reports, which showed  $^5\text{D}_0$  and  $^5\text{D}_1$  values of 17 830 and 19 450  $\text{cm}^{-1}$  respectively, based on CASSCF/XMCQDPT2/SO-CASSCF calculations.<sup>72</sup> This is also consistent with the previously reported experimental values of 17 300 and 19 000  $\text{cm}^{-1}$  for  $^5\text{D}_0$  and  $^5\text{D}_1$  of the  $\text{Eu}^{3+}$  ion.<sup>73</sup> The electronic structures of the BDC and DPA linkers, including the ground state ( $S_0$ ) and excited states ( $S_n$  and  $T_n$ ), were investigated using the CAS(10,10)SCF/NEVPT2 method with an active space of ten electrons in ten molecular orbitals

According to the CAS(10,10)SCF/NEVPT2 calculations for the DPA linker, the  $S_1$  electronic state is located at 31 194  $\text{cm}^{-1}$ , whereas the  $T_1$  electronic state appears at 23 828  $\text{cm}^{-1}$ . Therefore, the energy gap ( $S_1-T_1$ ) is 7366  $\text{cm}^{-1}$  which is not within the optimal range according to the Reinholdt rule. Following this empirical rule (Reinholdt rule), the energy gap between the  $S_1$  and  $T_1$  electronic states must be 5000  $\text{cm}^{-1}$  to ensure an efficient inter-system crossing (ISC)  $S_1 \rightarrow T_1$ .<sup>74</sup> The CAS(10,10)SCF/NEVPT2 calculations showed that the  $S_1$  and  $T_1$  electronic states of the BDC linker are located at 27 794 and 26 558  $\text{cm}^{-1}$ , respectively. Thus, the energy gap ( $S_1-T_1$ ) is 1236  $\text{cm}^{-1}$ .

In this regard, for both ligands (BDC and DPA), the  $S_1-T_1$  energy difference calculated at the CAS(10,10)SCF/NEVPT2 level of theory shows that the ISC process is totally efficient, according to the empirical rule. However, for  $\text{UiO-66}(\text{DPA})$ , it has been reported that after the PSM with  $\text{Eu}^{3+}$  (generating  $\text{Eu}^{3+}@ \text{UiO-66}(\text{DPA})$ ), a characteristic emission peak assigned to the  $\text{Eu}^{3+}$  ions appears. This suggests that the population of the  $T_1$  electronic state of the antenna and its subsequent energy transfer pathway may take another route from the commonly observed mechanism. We support this hypothesis with two arguments. First, the periodic DFT calculations indicate that the conduction band (CB) consists of a mixture of electronic states from BDC and DPA linkers just above the electronic state associated with  $\text{Eu}^{3+}$  ions. Second, the strong spin–orbit coupling (SOC) effect of  $\text{Eu}^{3+}$  ions in this material induces a mixture of electronic states with different multiplicities.

According to the Latva rule, an energy gap between 2500 and 4000  $\text{cm}^{-1}$  can facilitate efficient energy transfer from the  $T_1$  electronic state of the antenna to a resonance excited level of  $\text{Ln}^{3+}$  ions. This energy gap is adequate for an efficient ET channel when  $\Delta E(T \rightarrow \text{Ln}^*)$ , according to the Latva rule. A posterior analysis of CASSCF/NEVPT2 calculations showed that the  $T_1$  electronic state of the DPA antenna is located 6224  $\text{cm}^{-1}$  higher in energy than the  $\text{Eu}^{3+}$  ion  $^5\text{D}_0$  state (17 600  $\text{cm}^{-1}$ ). The  $T_1(\text{DPA})$  electronic state is located 3554  $\text{cm}^{-1}$  higher than the  $^5\text{D}_1$  electronic state (20 174  $\text{cm}^{-1}$ ) of the  $\text{Eu}^{3+}$  ion. The  $T_1$  electronic state of the BDC linker is located at 8988 and 6384  $\text{cm}^{-1}$  higher than the  $^5\text{D}_0$  and  $^5\text{D}_1$  electronic states of the  $\text{Eu}^{3+}$  ion. Based on these results, it can be considered that an energy transfer from the  $T_1$  electronic



state of the BDC or DPA linker to the emissive electronic state of  $^5D_0$  Eu ions has a low probability of occurring. Thus, the most important argument is that the most probable sensitization pathway involves the ISC process of DPA ( $S_1 \rightarrow T_1$ ), followed by an energy transfer channel that is activated from the  $T_1$  electronic state of the DPA linker to the  $^5D_1$  electronic state of  $Eu^{3+}$  ions,  $T_1$  (DPA)  $\rightarrow$   $^5D_1$  ( $Eu^{3+}$ ). Then, a vibrational relaxation (VR) from  $^5D_1$  can result in the emissive  $^5D_0$  state,  $^5D_1 \rightarrow$   $^5D_0$  ( $Eu^{3+}$ ). Additionally, the excited electronic states of the BDC antenna could enhance the population of the DPA antenna  $T_1$  electronic states through the ET process, as shown in Fig. 6. Finally, the radiative deactivation from  $^5D_0$  electronic states to the  $Eu^{3+}$   $^7F_J$  electronic states is produced (see Fig. 6).

A more detailed analysis of the excited electronic states was carried out. Table S2<sup>†</sup> lists the active orbitals, occupation numbers and low-lying excited electronic state configurations computed for the BDC antenna. As it is possible to appreciate, the  $S_1$  electronic state has 50% contribution of a configuration with  $^1(\pi \rightarrow \pi^*)$  character and 38% contribution of a configuration with  $^1(n \rightarrow \pi^*)$ , whereas the  $T_1$  electronic state of this antenna has 78% contribution of a configuration with  $^3(\pi \rightarrow \pi^*)$  character. Thus, multireference characteristics of these excited electronic states, which show a large change in the orbital type, could favor the ISC process ( $S_1$ (BDC)  $\rightarrow$   $T_1$ (BDC)), according to the El-Sayed rule.<sup>75,76</sup> However, in the case of the DPA antenna, as shown in Table S3,<sup>†</sup> the electronic configurations of the  $S_1$  and  $T_1$  electronic states do not indicate any change in the orbital type within the active space. The  $S_1$  electronic state has 50% contribution of a configuration with  $^1(\pi \rightarrow \pi^*)$  character and 20% contribution of a configuration with  $^1(n \rightarrow \pi^*)$ , whereas the  $T_1$  electronic state of the DPA antenna has 78% contribution of a configuration also with  $^3(\pi \rightarrow \pi^*)$  character. Thus, according to El-Sayed's rule, the electronic configurations of  $S_1$  and  $T_1$  are more likely to result in a slow intersystem crossing (ISC) due to the absence of a change in the orbital type.

Finally, the radiative and non-radiative processes involved in sensitization and ET channels were analyzed based on their rate constants. In the case of the BDC linker, the ISC rate  $k_{ISC}$  ( $S_1 \rightarrow T_1$ ) =  $6.00 \times 10^9$  s<sup>-1</sup> is larger than the fluorescence rate (three orders of magnitude) of  $k_F$  ( $S_1 \rightarrow S_0$ ) =  $4.28 \times 10^6$  s<sup>-1</sup>. As can be seen in Fig. 6, the ISC pathway from the DPA linker has an ISC rate of  $k_{ISC}$  ( $S_1 \rightarrow T_1$ ) =  $3.75 \times 10^9$  s<sup>-1</sup>, which is also three orders of magnitude greater than the fluorescence rate  $k_F$  ( $S_1 \rightarrow S_0$ ) =  $1.17 \times 10^6$  s<sup>-1</sup>. Thus, based on the rate constant of these photophysical processes for both linkers, it is likely that the population of the  $T_1$  electronic state occurs through an intersystem crossing (ISC) process before radiative decay. On the other hand, these calculations also reveal a slow phosphorescence ( $k_P$ ) rate for both linkers. As shown in Fig. 6, the DPA linker has a  $k_P$  ( $T_1 \rightarrow S_0$ ) value of  $2.07 \times 10^3$  s<sup>-1</sup>, while the BDC linker has a  $k_P$  ( $T_1 \rightarrow S_0$ ) value of  $4.43 \times 10^3$  s<sup>-1</sup>. Both linkers exhibit long-lived populations in their  $T_1$  electronic states, with nonradiative pathways such as ET to sensitize the  $Eu^{3+}$  ion. The LUMPAC software<sup>77</sup> was used to compute the energy transfer rates ( $k_{ET}$ ) and the back energy transfer rates ( $k_{BET}$ ). As illustrated in Fig. 6, ET rates  $k_{ET}$  that are within the order of  $10^4$ – $10^9$  s<sup>-1</sup> lead to a probable ET channel, both from the  $S_1$  and  $T_1$  electronic states. Although the  $T_1$  electronic state of the DPA antenna falls outside the energy range stipulated by Latva's rule, it still exhibits adequate energy transfer rates for  $T_1$  (DPA)  $\rightarrow$   $^5D_J$ ( $Eu^{3+}$ ). The  $k_{ET}(S_1 \rightarrow ^5D_1)$  =  $3.47 \times 10^5$  s<sup>-1</sup> and  $k_{ET}(S_1 \rightarrow ^5D_0)$  =  $3.24 \times 10^4$  s<sup>-1</sup> values are lower than the corresponding values for probable ET from the  $T_1$  electronic state, with  $k_{ET}(T_1 \rightarrow ^5D_1)$  =  $1.27 \times 10^9$  s<sup>-1</sup> and  $k_{ET}(T_1 \rightarrow ^5D_0)$  =  $5.61 \times 10^8$  s<sup>-1</sup>. Furthermore, the analysis of  $k_{BET}$  values indicates that the BET mechanism is not competitive in this system. The observed results support the proposed sensitization and emission mechanism between the DPA linker and the  $Eu^{3+}$  ion. The ET pathway from the ligand to the lanthanide dominates, as evidenced by the significantly lower and non-competitive BET rates:  $k_{BET}(^5D_1 \rightarrow T_1)$  =  $2.86 \times 10^{-3}$  s<sup>-1</sup> and  $k_{BET}(^5D_0 \rightarrow T_1)$  =  $3.09 \times$

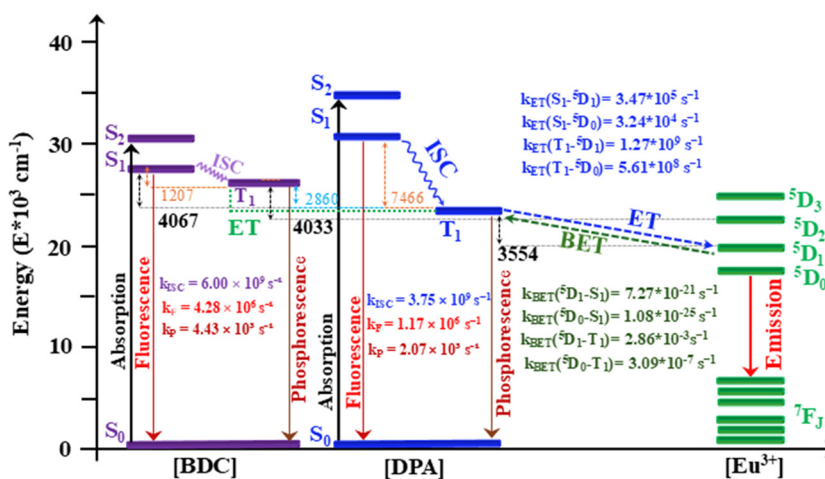


Fig. 6 The most likely sensitization and emission channels are depicted in this energy level diagram. Intersystem crossing, phosphorescence, fluorescence, energy transfer and back energy transfer rates are represented by the letters  $k_{ISC}$ ,  $k_P$ ,  $k_F$ ,  $k_{ET}$  and  $k_{BET}$ , respectively.



$10^{-7} \text{ s}^{-1}$ , both of which are too low to represent a predominant process. Likewise, the BET rates  $k_{\text{BET}}(^5\text{D}_1\text{-S}_1) = 7.27 \times 10^{-21} \text{ s}^{-1}$  and  $k_{\text{BET}}(^5\text{D}_0\text{-S}_1) = 1.08 \times 10^{-25} \text{ s}^{-1}$  confirm the negligible role of back transfer in this system.

### Luminescence quenching pathway in $\text{Hg}^{2+}@\text{UiO-66}(\text{DPA})$

The proposed sensing mechanism of  $\text{Eu}^{3+}@\text{UiO-66}(\text{DPA})^{22}$  is based on the high binding affinity of the DPA ligand for  $\text{Hg}^{2+}$  ions, which facilitates the replacement of  $\text{Eu}^{3+}$  by  $\text{Hg}^{2+}$ , resulting in luminescence quenching. The  $\text{Eu}^{3+}@\text{UiO-66}(\text{DPA})$  chemosensor exhibits a decrease in luminescence intensity (turn-off response) in the presence of  $\text{Hg}^{2+}$  ions, achieving a detection limit of 8.26 nM. According to the authors, in the presence of  $\text{Hg}^{2+}$ , the  $\text{Eu}^{3+}$  ions in  $\text{Eu}^{3+}@\text{UiO-66}(\text{DPA})$  are replaced by  $\text{Hg}^{2+}$  ions, leading to luminescence quenching as the concentration of  $\text{Hg}^{2+}$  increases. This proposed sensing mechanism aligns with previous reports. For instance, Hongliang Tan *et al.*<sup>78</sup> developed a lanthanide-based luminescent probe for  $\text{Hg}^{2+}$  detection using Eu-DPA chelates immobilized on  $\text{SiO}_2$  nanoparticles. This system demonstrated excellent selectivity towards  $\text{Hg}^{2+}$ , with a detection limit as low as 7.07 nM. In their study, the authors also suggested that the luminescence quenching is due to the replacement of  $\text{Eu}^{3+}$  by  $\text{Hg}^{2+}$ , primarily attributed to the significantly higher binding constant of  $\text{Hg}^{2+}$  ( $K = 10^{26.4}$ ) compared to  $\text{Eu}^{3+}$  ( $K = 10^{22.39}$ ).<sup>78</sup> Similar strategies leveraging the selectivity of these ligand (*i.e.*, DPA) interactions have been reported in other  $\text{Hg}^{2+}$  sensing systems. For instance, a gold nanoparticle-based sensor functionalized with DPA demonstrated exceptional selectivity for  $\text{Hg}^{2+}$  ions over other metal ions in aqueous solutions. In this system, the high affinity of DPA for  $\text{Hg}^{2+}$  supports stable complex formation, leading to reliable detection. Such findings highlight the critical role of ligand design and binding

affinity in achieving selectivity and sensitivity for  $\text{Hg}^{2+}$ , reinforcing the probability of the proposed mechanism in  $\text{Eu}^{3+}@\text{UiO-66}(\text{DPA})$ .

To investigate the luminescence quenching pathway in the  $\text{Hg}^{2+}@\text{UiO-66}(\text{DPA})$  system, the  $\text{S}_0$  and  $\text{S}_1$  electronic states were studied in terms of energy and structure. According to the Franck–Condon principle and selection rules, we support the hypothesis that, upon photoexcitation, the electron relaxes until reaching the first excited electronic state, presumably involved with the  $\text{Hg}^{2+}$  ions. Thus, in the first step, the vertical excitation of the  $\text{Hg}^{2+}@\text{UiO-66}(\text{DPA})$  (based on cluster models) was computed. This absorption spectrum displays three main transitions regarding the  $f$  values, one at 250 nm, a more intense one at 258 nm, and the last one at 306 nm.

The bands centered at 306 nm ( $f = 0.02$ ) correspond to  $\pi \rightarrow \pi^*$  electronic transitions from the HOMO to the LUMO+1, which are labeled as H and L+1 in Fig. 7. The MOs involved in this absorption band are localized at the bridging oxygen atoms of the  $[\text{Zr}_6(\text{OH})_4\text{O}_4]$  node and DPA linker; see the left panel in Fig. 7. The more intense bands are located at 258 nm ( $f = 1.02$ ) and are composed of  $\pi \rightarrow \pi^*$  electronic transitions (HOMO–3  $\rightarrow$  LUMO+2). These electronic transitions exhibit an inter-ligand charge-transfer (ILCT) character. The MOs involved in this absorption band are mainly localized on the BDC linker. The band at 250 nm is associated with a  $\pi \rightarrow \pi^*$  electronic transition (HOMO–3  $\rightarrow$  LUMO+1), which also presents an ILCT character; see Fig. 7.

In the second step, the probable emissive  $\text{S}_1$  state of  $\text{Hg}^{2+}@\text{UiO-66}(\text{DPA})$  was explored. This step begins with the optimization of the  $\text{S}_1$  electronic state, which was subsequently used as input data to calculate the electronic transitions associated with the emission spectrum by means of TD-DFT methods. All electronic transitions that correspond to the

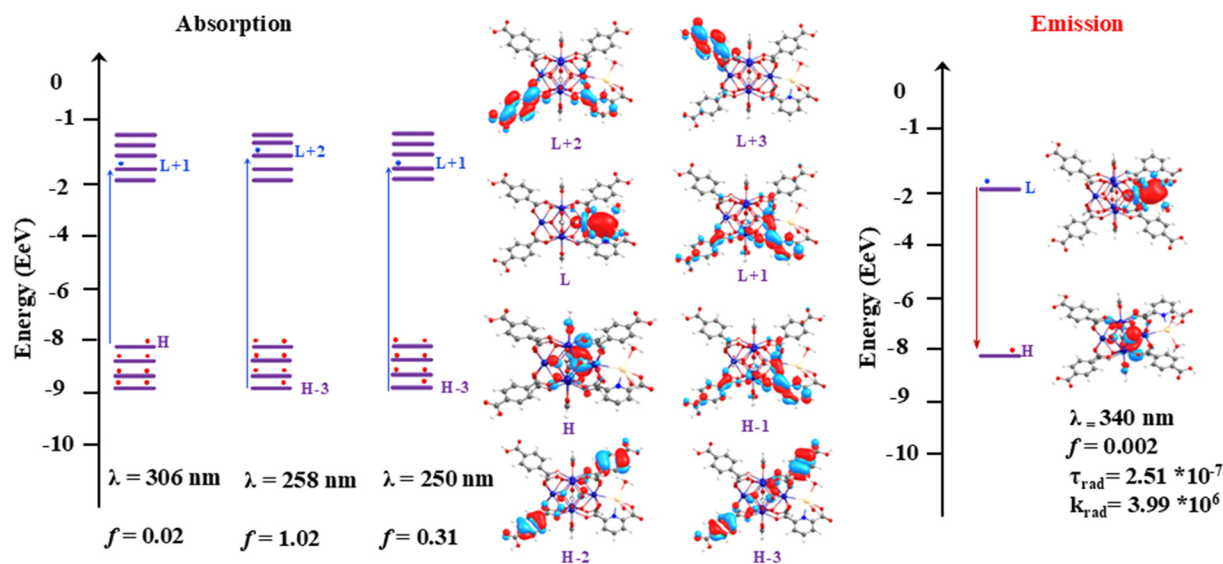


Fig. 7 Molecular orbital diagram based on the  $\text{S}_0$  (absorption) and  $\text{S}_1$  (emission) states of the  $\text{Hg}^{2+}@\text{UiO-66}(\text{DPA})$  system, where  $\lambda$  is the theoretical wavelength of absorption (left panel) and of emission (right panel), respectively;  $k_{\text{rad}}$  is the emission radiative rate;  $\tau_{\text{rad}}$  is the emission times; and  $f$  is the oscillator strength.



absorption process involve the molecular orbital just above the LUMO (orbital located on the Hg atom). Thus, considering the Franck–Condon principle and selection rules, it is more likely that, after excitation, the electron relaxes until reaching the  $S_1$  electronic state located on the Hg atom. Therefore, radiative deactivation could arise from the  $S_1$  electronic state, following Kasha's rule. The radiative rate ( $k_{\text{rad}}$ ) and radiative lifetime ( $\tau_{\text{rad}}$ ) computed for this electronic transition are in the range of fluorescence. As displayed in the right panel in Fig. 7,  $\tau_{\text{rad}}$  and  $k_{\text{rad}}$  present values which are in fluorescence for all calculations (less than  $10^{-6}$  seconds and  $10^6$  seconds $^{-1}$ , respectively).<sup>79</sup> However, if the intensity of these electronic transitions based on the  $f$  magnitude ( $f = 0.002$ ) is analyzed, the presence of Hg ions induces a “dark” excited state.

In summary, the most probable fluorescence quenching pathway of the  $\text{Hg}^{2+}@ \text{UiO-66(DPA)}$  system is supported by the hypothesis that after direct photoexcitation from the  $S_0$  electronic state, the electron relaxes to reach the first excited electronic state  $S_1$  located in the  $\text{Hg}^{2+}$  ion. For this reason, it is possible to state that the  $S_1$  electronic state decays to the  $S_0$  electronic state through a non-radiative mechanism.

## Conclusions

In summary, this report outlines a theoretical protocol that successfully provided an accurate explanation for the selective detection of  $\text{Hg}^{2+}$  ions using a  $\text{Eu}^{3+}$ -post functionalized UiO-66 (DPA) chemosensor. The elucidation of the sensing mechanism was addressed considering two points: the host–guest interaction (in this case, Hg is the host) and the photophysical properties of the material. First, the study of the  $\text{Eu}^{3+}@ \text{UiO-66(DPA)}$  system using rigorous CASSCF/NEVPT2 calculations was carried out to analyze the most probable sensitization and energy transfer pathway. This involves multireference *ab initio* methods using a truncated structural model (cluster model). In the  $\text{Eu}^{3+}@ \text{UiO-66(DPA)}$  system, CASSCF/NEVPT2 calculations predict that the most probable sensitization pathway is the DPA linker ( $S_1 \rightarrow T_1$ ) and DPA ( $T_1$ )  $\rightarrow \text{Eu}({}^5\text{D}_1)$ . Next, vibrational relaxation (VR) from the  ${}^5\text{D}_1$  state can lead to the population of the emissive  ${}^5\text{D}_0$  state, which subsequently emits from  ${}^7\text{F}_j$ . Furthermore, our investigation of the excited-state dynamics of the antenna supports the proposed sensitization and emission pathways. The intersystem crossing (ISC) process is significantly faster than the deactivation of the  $S_1$  electronic state *via* fluorescence ( $k_{\text{isc}}$  is three orders of magnitude greater than  $k_{\text{f}}$ ). This result confirms the feasibility of populating the  $T_1$  electronic state through ISC. The calculated rate constants for the phosphorescence process ( $k_{\text{p}}$ ) indicate that the DPA antenna exhibits a prolonged population in its  $T_1$  electronic state, which favors the energy transfer (ET) process to the  $\text{Eu}^{3+}$  ion. Lastly, the evaluation of radiative and non-radiative processes using the LUMPAC software demonstrates that ET is the predominant mechanism over back energy transfer (BET), further reinforcing our conclusions regarding the proposed emission mechanism for the  $\text{Eu}^{3+}@ \text{UiO-66(DPA)}$

system. From these results, an important finding is that the  $T_1$  electronic states of the BDC linker can reinforce the population of the  $T_1$  electronic states of the DPA antenna. The electronic density of states (DOS) analysis of  $\text{Eu}^{3+}@ \text{UiO-66(DPA)}$ , obtained *via* periodic DFT calculations, evidences the mixture of states of the linkers (BDC and DPA) and  $\text{Eu}^{3+}$  ions. This agrees with the sensitization and energy transfer mechanism proposed by the CASSCF/NEVPT2 results. Second, both the electronic and photophysical properties were assessed to determine the correlation between the chemosensor structure and the luminescence change prompted by the analyte. For the  $\text{Hg}^{2+}@ \text{UiO-66(DPA)}$  system, employing the optimized geometry of the  $S_0$  and  $S_1$  electronic states, the absorption and emission spectra were modelled based on the vertical transitions of the Franck–Condon and Kasha rules. The results indicate that following direct photoexcitation from the  $S_0$  state, the electron relaxes to the  $S_1$  state within the  $\text{Hg}^{2+}$  ion, subsequently decaying non-radiatively to the  $S_0$  state. For this system, the calculated emission time ( $\tau_{\text{rad}} = 2.51 \times 10^{-7}$ ) and radiative rate ( $k_{\text{rad}} = 3.99 \times 10^6$ ) are evidence of a probable deactivation of the  $S_1$  electronic state *via* the fluorescence process. However, the strength of the oscillator supports the hypothesis of a dark emissive state due to a low emission intensity ( $f$  magnitude of 0.002) and deactivation from the Hg molecular orbital. The proposed mechanism is also in good agreement with the electronic DOS analysis of  $\text{Hg}^{2+}@ \text{UiO-66(DPA)}$  obtained *via* periodic DFT. DOS analysis evidences an overlap of states of both linkers (BDC and DPA) and  $\text{Hg}^{2+}$  ions at the edge of the conduction band, which agrees with the turn-off induced by  $\text{Hg}^{2+}$  ions. These findings are particularly relevant for advancing the design of MOF-based sensors, enhancing their efficacy in selective  $\text{Hg}^{2+}$  detection. Finally, we accomplished a computational procedure combining a multireference *ab initio* method with periodic DFT calculations which are not frequently taken into account by previous reports. Thus, this methodology is accurate to be applied to different lanthanide-doped MOF chemosensor systems to study the electronic properties that govern the sensing mechanisms, or to design new sensors based on MOFs.

## Data availability

Data are available upon request from the authors.

## Conflicts of interest

There are no conflicts to declare.

## Acknowledgements

The authors are thankful for FONDECYT projects 1231194, 1241917, and 1220442 and ANID Postdoctoral 3230141 (ANID/FONDAP/1523A0006). This material is based on the work supported by the Air Force Office of Scientific Research under award number FA8655-25-1-8759.



## References

- Z. Ali, R. Ullah, M. Tuzen, S. Ullah, A. Rahim and T. A. Saleh, Colorimetric Sensing of Heavy Metals on Metal Doped Metal Oxide Nanocomposites: A Review, *Trends Environ. Anal. Chem.*, 2023, **37**, e00187, DOI: [10.1016/J.TEAC.2022.E00187](https://doi.org/10.1016/J.TEAC.2022.E00187).
- S. Mishra, R. N. Bharagava, N. More, A. Yadav, S. Zainith, S. Mani and P. Chowdhary, Heavy Metal Contamination: An Alarming Threat to Environment and Human Health, in *Environmental Biotechnology: For Sustainable Future*, Springer, Singapore, 2019, pp. 103–125. DOI: [10.1007/978-981-10-7284-0\\_5](https://doi.org/10.1007/978-981-10-7284-0_5).
- L. A. Malik, A. Bashir, A. Qureashi and A. H. Pandith, Detection and Removal of Heavy Metal Ions: A Review, *Environ. Chem. Lett.*, 2019, **17**(4), 1495–1521, DOI: [10.1007/s10311-019-00891-z](https://doi.org/10.1007/s10311-019-00891-z).
- J. F. Olorunyomi, S. T. Geh, R. A. Caruso and C. M. Doherty, Metal-Organic Frameworks for Chemical Sensing Devices, *Mater. Horiz.*, 2021, **8**(9), 2387–2419, DOI: [10.1039/d1mh00609f](https://doi.org/10.1039/d1mh00609f).
- T. Elias Abi-Ramia Silva, F. Burisch and A. T. Güntner, Gas Sensing for Space: Health and Environmental Monitoring, *TrAC, Trends Anal. Chem.*, 2024, **177**, 117790, DOI: [10.1016/j.trac.2024.117790](https://doi.org/10.1016/j.trac.2024.117790).
- X.-Y. Xu and B. Yan, Fabrication and Application of a Ratiometric and Colorimetric Fluorescent Probe for Hg 2+ Based on Dual-Emissive Metal–Organic Framework Hybrids with Carbon Dots and Eu 3+, *J. Mater. Chem. C*, 2016, **4**(7), 1543–1549, DOI: [10.1039/C5TC04002G](https://doi.org/10.1039/C5TC04002G).
- J. R. Askim, M. Mahmoudi and K. S. Suslick, Optical Sensor Arrays for Chemical Sensing: The Optoelectronic Nose, *Chem. Soc. Rev.*, 2013, **42**(22), 8649–8682, DOI: [10.1039/c3cs60179j](https://doi.org/10.1039/c3cs60179j).
- L. Guan, Z. Jiang, Y. Cui, Y. Yang, D. Yang and G. Qian, An MOF-Based Luminescent Sensor Array for Pattern Recognition and Quantification of Metal Ions, *Adv. Opt. Mater.*, 2021, **9**(9), 1–7, DOI: [10.1002/adom.202002180](https://doi.org/10.1002/adom.202002180).
- C. W. Huang, C. Lin, M. K. Nguyen, A. Hussain, X. T. Bui and H. H. Ngo, A Review of Biosensor for Environmental Monitoring: Principle, Application, and Corresponding Achievement of Sustainable Development Goals, *Bioengineered*, 2023, **14**(1), 58–80, DOI: [10.1080/21655979.2022.2095089](https://doi.org/10.1080/21655979.2022.2095089).
- L. Yu, Q. Zheng, H. Wang, C. Liu, X. Huang and Y. Xiao, Double-Color Lanthanide Metal–Organic Framework Based Logic Device and Visual Ratiometric Fluorescence Water Microsensor for Solid Pharmaceuticals, *Anal. Chem.*, 2020, **92**(1), 1402–1408, DOI: [10.1021/acs.analchem.9b04575](https://doi.org/10.1021/acs.analchem.9b04575).
- Y. Zhao, M. Liu, S. Zhou, Z. Yan, J. Tian, Q. Zhang and Z. Yao, Smartphone-Assisted Ratiometric Sensing Platform for on-Site Tetracycline Determination Based on Europium Functionalized Luminescent Zr-MOF, *Food Chem.*, 2023, **425**, 136449, DOI: [10.1016/j.foodchem.2023.136449](https://doi.org/10.1016/j.foodchem.2023.136449).
- T. Wang, J. Zhang, Y. Wu, S. Wang, X. Jiang, Z. Zhang and S. Li, Smartphone - Integrated Ratiometric Fluorescence Sensing Platform Based on Bimetallic Metal – Organic Framework Nanowires for Anthrax Biomarker Detection, *Microchim. Acta*, 2023, **190**(12), 1–9, DOI: [10.1007/s00604-023-06065-7](https://doi.org/10.1007/s00604-023-06065-7).
- K. F. Kayani, N. N. Mohammad, D. A. Kader and S. J. Mohammed, Ratiometric Lanthanide Metal-Organic Frameworks (MOFs) for Smartphone-Assisted Visual Detection of Food Contaminants and Water: A Review, *ChemistrySelect*, 2023, **8**, 202303472, DOI: [10.1002/slct.202303472](https://doi.org/10.1002/slct.202303472).
- X. Zeng, J. Hu, M. Zhang, F. Wang, L. Wu and X. Hou, Visual Detection of Fluoride Anions Using Mixed Lanthanide Metal – Organic Frameworks with a Smartphone, *Anal. Chem.*, 2020, **92**, 2097–2102, DOI: [10.1021/acs.analchem.9b04598](https://doi.org/10.1021/acs.analchem.9b04598).
- X. Zhang, Z. Li, Y. Zhang, C. Jiao, H. Zheng, Y. Zhu and Z. Sun, Ultrastable Lanthanide Metal – Organic Frameworks for Smartphone-Assisted Ratiometric Fluorescent Sensing of Toluenediamines and Tunable Luminescence, *Inorg. Chem.*, 2024, **63**, 16418–16428, DOI: [10.1021/acs.inorgchem.4c02461](https://doi.org/10.1021/acs.inorgchem.4c02461).
- W. Wu, Y. Li, P. Song, Q. Xu, N. Long, P. Li, L. Zhou, B. Fu, J. Wang and W. Kong, Metal-Organic Framework (MOF)-Based Sensors for Exogenous Contaminants in Food: Mechanisms, Advances, and Prospects, *Trends Food Sci. Technol.*, 2023, **138**, 238–271, DOI: [10.1016/j.tifs.2023.06.016](https://doi.org/10.1016/j.tifs.2023.06.016).
- H. Y. Li, S. N. Zhao, S. Q. Zang and J. Li, Functional Metal-Organic Frameworks as Effective Sensors of Gases and Volatile Compounds, *Chem. Soc. Rev.*, 2020, **49**(17), 6364–6401, DOI: [10.1039/c9cs00778d](https://doi.org/10.1039/c9cs00778d).
- M. D. Allendorf, C. A. Bauer, R. K. Bhakta and R. J. T. Houk, Luminescent Metal-Organic Frameworks, *Chem. Soc. Rev.*, 2009, **38**(5), 1330–1352, DOI: [10.1039/b802352m](https://doi.org/10.1039/b802352m).
- W. P. Lustig, S. Mukherjee, N. D. Rudd, A. V. Desai, J. Li and S. K. Ghosh, Metal–Organic Frameworks: Functional Luminescent and Photonic Materials for Sensing Applications, *Chem. Soc. Rev.*, 2017, **46**(11), 3242–3285, DOI: [10.1039/C6CS00930A](https://doi.org/10.1039/C6CS00930A).
- L. Fan, D. Zhao, B. Li, F. Wang, Y. Deng, Y. Peng, X. Wang and X. Zhang, Luminescent Binuclear Zinc(II) Organic Framework as Bifunctional Water-Stable Chemosensor for Efficient Detection of Antibiotics and Cr(VI) Anions in Water, *Spectrochim. Acta, Part A*, 2022, **264**, 120232, DOI: [10.1016/j.saa.2021.120232](https://doi.org/10.1016/j.saa.2021.120232).
- J. Jin, J. Xue, Y. Liu, G. Yang and Y. Y. Wang, Recent Progresses in Luminescent Metal-Organic Frameworks (LMOFs) as Sensors for the Detection of Anions and Cations in Aqueous Solution, *Dalton Trans.*, 2021, **50**(6), 1950–1972, DOI: [10.1039/d0dt03930f](https://doi.org/10.1039/d0dt03930f).
- Z. Xiaoxiong, Z. Wenjun, L. Cuiliu, Q. Xiaohong and Z. Chengyu, Eu 3+ -Postdoped UiO-66-Type Metal–Organic Framework as a Luminescent Sensor for Hg 2+ Detection in Aqueous Media, *Inorg. Chem.*, 2019, **58**(6), 3910–3915, DOI: [10.1021/acs.inorgchem.8b03555](https://doi.org/10.1021/acs.inorgchem.8b03555).



- 23 L. Fan, D. Zhao, B. Li, X. Chen, F. Wang, Y. Deng, Y. Niu and X. Zhang, An Exceptionally Stable Luminescent Cadmium(II) Metal-Organic Framework as a Dual-Functional Chemosensor for Detecting Cr(VI) Anions and Nitro-Containing Antibiotics in Aqueous Media, *CrystEngComm*, 2021, **23**(5), 1218–1225, DOI: [10.1039/d0ce01721c](https://doi.org/10.1039/d0ce01721c).
- 24 T. Zhang, H. Chen, H. Lv, Q. Li and X. Zhang, Nanochannel-Based Heterometallic {ZnIIHoIII}-Organic Framework with High Catalytic Activity for the Chemical Fixation of CO<sub>2</sub>, *RSC Adv.*, 2021, **11**(16), 9731–9739, DOI: [10.1039/d1ra00590a](https://doi.org/10.1039/d1ra00590a).
- 25 G. Li and C. Tong, Dual-Functional Lanthanide Metal Organic Frameworks for Visual and Ultrasensitive Ratiometric Fluorescent Detection of Phosphate Based on Aggregation-Induced Energy Transfer, *Anal. Chim. Acta*, 2020, **1133**, 11–19, DOI: [10.1016/j.aca.2020.07.066](https://doi.org/10.1016/j.aca.2020.07.066).
- 26 Y. Hidalgo-Rosa, M. A. Treto-Suárez, E. Schott, X. Zarate and D. Páez-Hernández, Sensing Mechanism Elucidation of a Europium(III) Metal–Organic Framework Selective to Aniline: A Theoretical Insight by Means of Multiconfigurational Calculations, *J. Comput. Chem.*, 2020, **41**(22), 1956–1964, DOI: [10.1002/jcc.26365](https://doi.org/10.1002/jcc.26365).
- 27 J. Dong, D. Zhao, Y. Lu and W.-Y. Sun, Photoluminescent Metal-Organic Frameworks and Their Application for Sensing Biomolecules, *J. Mater. Chem. A*, 2019, **7**, 22744–22767, DOI: [10.1039/C9TA07022B](https://doi.org/10.1039/C9TA07022B).
- 28 B. Yan, Lanthanide-Functionalized Metal-Organic Framework Hybrid Systems to Create Multiple Luminescent Centers for Chemical Sensing, *Acc. Chem. Res.*, 2017, **50**(11), 2789–2798, DOI: [10.1021/acs.accounts.7b00387](https://doi.org/10.1021/acs.accounts.7b00387).
- 29 S. Zhao, G. Wang and D. Poelman, Luminescent Lanthanide MOFs : A Unique Platform for Chemical Sensing, *Materials*, 2018, **11**(4), 572, DOI: [10.3390/ma11040572](https://doi.org/10.3390/ma11040572).
- 30 Y. Cui, Y. Yue, G. Qian and B. Chen, Luminescent Functional Metal–Organic Frameworks, *Chem. Rev.*, 2012, **112**(2), 1126–1162, DOI: [10.1021/cr200101d](https://doi.org/10.1021/cr200101d).
- 31 S. M. Cohen, Postsynthetic Methods for the Functionalization of Metal-Organic Frameworks, *Chem. Rev.*, 2012, **112**(2), 970–1000, DOI: [10.1021/cr200179u](https://doi.org/10.1021/cr200179u).
- 32 S. Mandal, S. Natarajan, P. Mani and A. Pankajakshan, Post-Synthetic Modification of Metal–Organic Frameworks Toward Applications, *Adv. Funct. Mater.*, 2021, **31**(4), 1–22, DOI: [10.1002/adfm.202006291](https://doi.org/10.1002/adfm.202006291).
- 33 S. Mandal, S. Natarajan, P. Mani and A. Pankajakshan, Post-Synthetic Modification of Metal–Organic Frameworks Toward Applications, *Adv. Funct. Mater.*, 2021, **31**(4), 1–22, DOI: [10.1002/adfm.202006291](https://doi.org/10.1002/adfm.202006291).
- 34 Y. N. Zeng, H. Q. Zheng, J. F. Gu, G. J. Cao, W. E. Zhuang, J. D. Lin, R. Cao and Z. J. Lin, Dual-Emissive Metal-Organic Framework as a Fluorescent “Switch” for Ratiometric Sensing of Hypochlorite and Ascorbic Acid, *Inorg. Chem.*, 2019, **58**(19), 13360–13369, DOI: [10.1021/acs.inorgchem.9b02251](https://doi.org/10.1021/acs.inorgchem.9b02251).
- 35 J. N. Hao and B. Yan, Ag<sup>+</sup>-Sensitized Lanthanide Luminescence in Ln<sup>3+</sup> Post-Functionalized Metal-Organic Frameworks and Ag<sup>+</sup> Sensing, *J. Mater. Chem. A*, 2015, **3**(9), 4788–4792, DOI: [10.1039/c4ta06462c](https://doi.org/10.1039/c4ta06462c).
- 36 S. Yang, Z. Zhou, Z. Zhao, J. Liu, Y. Sun, Y. Zhang, E. Gao, M. Zhu and S. Wu, Synthesis of Multi-Emission MOF Composites for Multi-Dimensional Sensing Application, *Microchem. J.*, 2024, **196**, 109660, DOI: [10.1016/j.microc.2023.109660](https://doi.org/10.1016/j.microc.2023.109660).
- 37 C. Xia, Y. Xu, M. M. Cao, Y. P. Liu, J. F. Xia, D. Y. Jiang, G. H. Zhou, R. J. Xie, D. F. Zhang and H. L. Li, A Selective and Sensitive Fluorescent Probe for Bilirubin in Human Serum Based on Europium(III) Post-Functionalized Zr(IV)-Based MOFs, *Talanta*, 2020, **212**, 120795, DOI: [10.1016/j.talanta.2020.120795](https://doi.org/10.1016/j.talanta.2020.120795).
- 38 Z. Yu, S. Kang, M. Tai, J. Wang, Q. Tian, D. Jin and L. Wang, Synthesis, Modulation, and Characterization of Ln<sup>3+</sup> Ions Doped Metal–organic Frameworks for WLED Applications, *Dyes Pigm.*, 2023, **209**, 110897, DOI: [10.1016/j.dyepig.2022.110897](https://doi.org/10.1016/j.dyepig.2022.110897).
- 39 H. Liu, Y. Liu, Y. Meng, X. Shi, J. Sun, L. Zhao, D. Chen, H. Hao, D. Li, J. Dou and J. Han, Di-Functional Luminescent Sensors Based on Y<sup>3+</sup> + doped Eu<sup>3+</sup> + and Tb<sup>3+</sup> + coordination Polymers: Fast Response and Visible Detection of Cr<sup>3+</sup>, Fe<sup>3+</sup> + ions in Aqueous Solutions and Acetone, *RSC Adv.*, 2020, **10**(53), 32232–32240, DOI: [10.1039/d0ra06407f](https://doi.org/10.1039/d0ra06407f).
- 40 M. J. Beltrán-Leiva, P. Cantero-López, C. Zúñiga, A. Bulhões-Figueira, D. Páez-Hernández and R. Arratia-Pérez, Theoretical Method for an Accurate Elucidation of Energy Transfer Pathways in Europium(III) Complexes with Dipyridophenazine (Dppz) Ligand: One More Step in the Study of the Molecular Antenna Effect, *Inorg. Chem.*, 2017, **56**(15), 9200–9208, DOI: [10.1021/acs.inorgchem.7b01221](https://doi.org/10.1021/acs.inorgchem.7b01221).
- 41 J. L. Mancuso, A. M. Mroz, K. N. Le and C. H. Hendon, Electronic Structure Modeling of Metal-Organic Frameworks, *Chem. Rev.*, 2020, **120**(16), 8641–8715, DOI: [10.1021/acs.chemrev.0c00148](https://doi.org/10.1021/acs.chemrev.0c00148).
- 42 Y. Hidalgo-Rosa, J. Santoyo-Flores, M. A. Treto-Suárez, E. Schott, D. Páez-Hernández and X. Zarate, Tuning the Sensitization Pathway T<sub>1</sub> → 5 D<sub>J</sub> in Eu-Based MOF through Modification of the Antenna Ligand. A Theoretical Approach via Multiconfigurational Quantum Calculations, *J. Lumin.*, 2023, **260**, 119896, DOI: [10.1016/j.jlumin.2023.119896](https://doi.org/10.1016/j.jlumin.2023.119896).
- 43 Y. Hidalgo-Rosa, K. Mena-Ulecia, M. A. Treto-Suárez, E. Schott, D. Páez-Hernández and X. Zarate, Expanding the Knowledge of the Selective-Sensing Mechanism of Nitro Compounds by Luminescent Terbium Metal-Organic Frameworks through Multiconfigurational Ab Initio Calculations, *J. Phys. Chem. A*, 2022, **126**(39), 7040–7050.
- 44 Y. Hidalgo-Rosa, K. Mena-Ulecia, M. A. Treto-Suárez, E. Schott, D. Páez-Hernández and X. Zarate, Insights into the Selective Sensing Mechanism of a Luminescent Cd(II)-Based MOF Chemosensor toward NACs: Roles of the Host–Guest Interactions and PET Processes, *J. Mater. Sci.*, 2021, **56**(24), 13684–13704, DOI: [10.1007/s10853-021-06196-3](https://doi.org/10.1007/s10853-021-06196-3).



- 45 Y. Hidalgo-Rosa, M. Saavedra-Torres, B. D. Koivisto, M. A. Treto-Suárez, D. Páez-Hernández, X. Zarate and E. Schott, Rare-Earth-Based Metal–Organic Frameworks with Improved Visible-Light-Harvesting Properties: A Quantum Chemistry Study, *J. Mater. Sci.*, 2023, **58**(21), 8862–8877, DOI: [10.1007/s10853-023-08581-6](https://doi.org/10.1007/s10853-023-08581-6).
- 46 Y. Hidalgo-Rosa, M. A. Treto-Suárez, E. Schott, X. Zarate and D. Páez-Hernández, Sensing Mechanism Elucidation of a Chemosensor Based on a Metal–Organic Framework Selective to Explosive Aromatic Compounds, *Int. J. Quantum Chem.*, 2020, **120**(23), e26404, DOI: [10.1002/qua.26404](https://doi.org/10.1002/qua.26404).
- 47 Z. Xiaoxiong, Z. Wenjun, L. Cuiliu, Q. Xiaohong and Z. Chengyu, Eu<sup>3+</sup>-Postdoped UiO-66-Type Metal–Organic Framework as a Luminescent Sensor for Hg<sup>2+</sup> Detection in Aqueous Media, *Inorg. Chem.*, 2019, **58**(6), 3910–3915, DOI: [10.1021/acs.inorgchem.8b03555](https://doi.org/10.1021/acs.inorgchem.8b03555).
- 48 J. Guo, C. Dong, X. Zhang, Y. Liu, Y. Leng, G. Wang and Z. Chen, Colorimetric Sensors Constructed with One Dimensional PtNi Nanowire and Pt Nanowire Nanozymes for Hg<sup>2+</sup> Detection, *Anal. Chim. Acta*, 2024, **1321**, 343039, DOI: [10.1016/j.aca.2024.343039](https://doi.org/10.1016/j.aca.2024.343039).
- 49 Y. Zhao and D. Li, Lanthanide-Functionalized Metal–Organic Frameworks as Ratiometric Luminescent Sensors, *J. Mater. Chem. C*, 2020, **8**(37), 12739–12754, DOI: [10.1039/d0tc03430d](https://doi.org/10.1039/d0tc03430d).
- 50 M. Treger, A. Hannebauer, A. Schaate, J. L. Budde, P. Behrens and A. M. Schneider, Tuning the Optical Properties of the Metal–Organic Framework UiO-66 via Ligand Functionalization, *Phys. Chem. Chem. Phys.*, 2023, **25**(8), 6333–6341, DOI: [10.1039/d2cp03746g](https://doi.org/10.1039/d2cp03746g).
- 51 E. A. Dolgoplova, A. J. Brandt, O. A. Ejegbawo, A. S. Duke, T. D. Maddumapatabandi, R. P. Galhenage, B. W. Larson, O. G. Reid, S. C. Ammal, A. Heyden, M. Chandrashekar, V. Stavila, D. A. Chen and N. B. Shustova, Electronic Properties of Bimetallic Metal–Organic Frameworks (MOFs): Tailoring the Density of Electronic States through MOF Modularity, *J. Am. Chem. Soc.*, 2017, **139**(14), 5201–5209, DOI: [10.1021/jacs.7b01125](https://doi.org/10.1021/jacs.7b01125).
- 52 J.-C. Jin, J. Wu, Y.-X. He, B.-H. Li, J.-Q. Liu, R. Prasad, A. Kumar and S. R. Batten, A 3D Luminescent Zn(ii) MOF for the Detection of High Explosives and the Degradation of Organic Dyes: An Experimental and Computational Study, *CrystEngComm*, 2017, **19**(43), 6464–6472, DOI: [10.1039/C7CE01341H](https://doi.org/10.1039/C7CE01341H).
- 53 B. Sun, T. Tao, L. Liu, R. Ding and Y. Mao, Electron Transfer Facilitated by  $\pi$ - $\pi$  Stacking during the Nitrobenzene Recognition Process of an MOF Sensor, *J. Phys. Chem. C*, 2021, **125**(22), 12433–12440, DOI: [10.1021/acs.jpcc.1c02942](https://doi.org/10.1021/acs.jpcc.1c02942).
- 54 L. Liu, R. Ding, Y. Mao and B. Sun, Theoretical Investigations on the Nitro-Explosive Sensing Process of a MOF Sensor: Roles of Hydrogen Bond and  $\pi$ - $\pi$  Stacking, *Chem. Phys. Lett.*, 2022, **793**, 139393, DOI: [10.1016/j.cplett.2022.139393](https://doi.org/10.1016/j.cplett.2022.139393).
- 55 S. Ghosh, R. Lipin, A. Ngoipala, N. Ruser, D. M. Venturi, A. Rana, M. Vandichel and S. Biswas, Hf-Based MOF for Rapid and Selective Sensing of a Nerve Agent Simulant and an Aminophenol: Insights from Experiments and Theory, *Inorg. Chem.*, 2023, **62**(36), 14632–14646, DOI: [10.1021/acs.inorgchem.3c01777](https://doi.org/10.1021/acs.inorgchem.3c01777).
- 56 D. Yan, Y. Tang, H. Lin and D. Wang, Tunable Two-Color Luminescence and Host–Guest Energy Transfer of Fluorescent Chromophores Encapsulated in Metal–Organic Frameworks, *Sci. Rep.*, 2014, **4**(1), 4337, DOI: [10.1039/C3TA14328G](https://doi.org/10.1039/C3TA14328G).
- 57 Y. Luo, D. Lei, M. Li, Y. Ge, J. Li, B. Zu, J. Yao and X. Dou, Fluorophore Branching Boosted Photo-Induced Energy Transfer in UiO-66 for Ultrasensitive and Instant Hydrazine Sensing, *J. Mater. Chem. A*, 2024, **12**(20), 12088–12097, DOI: [10.1039/d4ta01549e](https://doi.org/10.1039/d4ta01549e).
- 58 K. Leong, M. E. Foster, B. M. Wong, E. D. Spoerke, D. Van Gough, J. C. Deaton and M. D. Allendorf, Energy and Charge Transfer by Donor–Acceptor Pairs Confined in a Metal–Organic Framework: A Spectroscopic and Computational Investigation, *J. Mater. Chem. A*, 2014, **2**(10), 3389–3398, DOI: [10.1039/C3TA14328G](https://doi.org/10.1039/C3TA14328G).
- 59 M. Y. Toriyama, A. M. Ganose, M. Dylla, S. Anand, J. Park, M. K. Brod, J. M. Munro, K. A. Persson, A. Jain and G. J. Snyder, How to Analyse a Density of States, *Mater. Today Electron.*, 2022, **1**, 100002, DOI: [10.1016/j.mtelec.2022.100002](https://doi.org/10.1016/j.mtelec.2022.100002).
- 60 K. Hendrickx, J. J. Joos, A. De Vos, D. Poelman, P. F. Smet, V. Van Speybroeck, P. Van Der Voort and K. Lejaeghere, Exploring Lanthanide Doping in UiO-66: A Combined Experimental and Computational Study of the Electronic Structure, *Inorg. Chem.*, 2018, **57**(9), 5463–5474, DOI: [10.1021/acs.inorgchem.8b00425](https://doi.org/10.1021/acs.inorgchem.8b00425).
- 61 F. Yuan, H. X. Ma, C. M. Yuan, C. S. Zhou, H. M. Hu, A. Kumar and M. Muddassir, Syntheses of a Series of Lanthanide Metal–Organic Frameworks for Efficient UV-Light-Driven Dye Degradation: Experiment and Simulation, *CrystEngComm*, 2021, **23**(12), 2404–2413, DOI: [10.1039/d0ce01245a](https://doi.org/10.1039/d0ce01245a).
- 62 X. P. Wu, L. Gagliardi and D. G. Truhlar, Cerium Metal–Organic Framework for Photocatalysis, *J. Am. Chem. Soc.*, 2018, **140**(25), 7904–7912, DOI: [10.1021/jacs.8b03613](https://doi.org/10.1021/jacs.8b03613).
- 63 S. Yu, G. Jing, S. Li, Z. Li and X. Ju, Tuning the Hydrogen Storage Properties of MOF-650: A Combined DFT and GCMC Simulations Study, *Int. J. Hydrogen Energy*, 2020, **45**(11), 6757–6764, DOI: [10.1016/j.ijhydene.2019.12.114](https://doi.org/10.1016/j.ijhydene.2019.12.114).
- 64 L. Zhao, X. Ren, Y. Du, Z. Gao, H. Ma, H. Wang, Y. Li, Q. Wei, H. Ju and D. Wu, Europium-Based Metal–Organic Framework with N–H $\cdots$  $\pi$  Interaction and Intramolecular Energy Transfer Mechanisms for Self-Electrochemiluminescence, *Adv. Funct. Mater.*, 2024, **2410886**, 1–7, DOI: [10.1002/adfm.202410886](https://doi.org/10.1002/adfm.202410886).
- 65 J. J. Santoyo-Flores and D. Páez-Hernández, Theoretical Study of 8-Hydroxyquinoline Derivatives as Potential Antennas in Lanthanide Complexes: Photophysical Properties and Elucidation of Energy Transfer Pathways, *Int. J. Quantum Chem.*, 2022, **122**(10), e26880, DOI: [10.1002/qua.26880](https://doi.org/10.1002/qua.26880).



- 66 C. Celis-Barros, D. Páez-Hernández, M. J. Beltrán-Leiva and R. Arratia-Perez, Ab Initio Calculations of Heavy-Actinide Hexahalide Compounds: Do These Heavy Actinides Behave like Their Isoelectronic Lanthanide Analogues?, *Phys. Chem. Chem. Phys.*, 2018, **20**(6), 4038–4049, DOI: [10.1039/c7cp06585j](https://doi.org/10.1039/c7cp06585j).
- 67 Y. Hidalgo-Rosa, K. Mena-Ulecia, M. A. Treto-Suárez, E. Schott, D. Páez-Hernández and X. Zarate, Expanding the Knowledge of the Selective-Sensing Mechanism of Nitro Compounds by Luminescent Terbium Metal-Organic Frameworks through Multiconfigurational Ab Initio Calculations, *J. Phys. Chem. A*, 2022, **126**(39), 7040–7050, DOI: [10.1021/ACS.jpca.2c05468](https://doi.org/10.1021/ACS.jpca.2c05468).
- 68 F. Kossoski and P. F. Loos, State-Specific Configuration Interaction for Excited States, *J. Chem. Theory Comput.*, 2023, **19**(8), 2258–2269, DOI: [10.1021/acs.jctc.3c00057](https://doi.org/10.1021/acs.jctc.3c00057).
- 69 Y. Horiuchi, T. Toyao, M. Saito, K. Mochizuki, M. Iwata, H. Higashimura, M. Anpo and M. Matsuoka, Visible-Light-Promoted Photocatalytic Hydrogen Production by Using an Amino-Functionalized Ti(IV) Metal-Organic Framework, *J. Phys. Chem. C*, 2012, **116**(39), 20848–20853, DOI: [10.1021/jp3046005](https://doi.org/10.1021/jp3046005).
- 70 M. A. Nasalevich, C. H. Hendon, J. G. Santaclara, K. Svane, B. Van Der Linden, S. L. Veber, M. V. Fedin, A. J. Houtepen, M. A. Van Der Veen, F. Kapteijn, A. Walsh and J. Gascon, Electronic Origins of Photocatalytic Activity in D0 Metal Organic Frameworks, *Sci. Rep.*, 2016, **6**, 1–9, DOI: [10.1038/srep23676](https://doi.org/10.1038/srep23676).
- 71 A. De Vos, K. Hendrickx, P. Van Der Voort, V. Van Speybroeck and K. Lejaeghere, Missing Linkers: An Alternative Pathway to UiO-66 Electronic Structure Engineering, *Chem. Mater.*, 2017, **29**(7), 3006–3019, DOI: [10.1021/acs.chemmater.6b05444](https://doi.org/10.1021/acs.chemmater.6b05444).
- 72 Z. Abbas, S. Dasari, M. J. Beltrán-Leiva, P. Cantero-López, D. Páez-Hernández, R. Arratia-Pérez, R. J. Butcher and A. K. Patra, Luminescent Europium(III) and Terbium(III) Complexes of  $\beta$ -Diketonate and Substituted Terpyridine Ligands: Synthesis, Crystal Structures and Elucidation of Energy Transfer Pathways, *New J. Chem.*, 2019, **43**(38), 15139–15152, DOI: [10.1039/c9nj02838b](https://doi.org/10.1039/c9nj02838b).
- 73 E. M. Gomes, J. P. De Oliveira Silva, M. V. Colaço, A. Cuin, D. F. Franco, S. L. Scarpari, D. O. De Souza, M. S. Ferreira, R. O. Freire and L. F. Marques, Two Highly Photoluminescent Eu<sup>3+</sup>  $\beta$ -Diketonates Complexes with  $\epsilon$ -Caprolactam as Ancillary Ligands: From Synthesis to the First Example as Gunshot Residue Markers, *Opt. Mater.*, 2023, **137**, 113527, DOI: [10.1016/j.optmat.2023.113527](https://doi.org/10.1016/j.optmat.2023.113527).
- 74 F. J. Steemers, W. Verboom, D. N. Reinhoudt, E. B. van der Tol and J. W. Verhoeven, New Sensitizer-Modified Calix[4] Arenes Enabling Near-UV Excitation of Complexed Luminescent Lanthanide Ions, *J. Am. Chem. Soc.*, 1995, **117**(37), 9408–9414, DOI: [10.1021/ja00142a004](https://doi.org/10.1021/ja00142a004).
- 75 M. A. El-Sayed, The Triplet State: Its Radiative and Nonradiative Properties, *Acc. Chem. Res.*, 1968, **1**(1), 8–16, DOI: [10.1021/ar50001a002](https://doi.org/10.1021/ar50001a002).
- 76 M. A. El-Sayed, Spin-Orbit Coupling and the Radiationless Processes in Nitrogen Heterocyclics, *J. Chem. Phys.*, 1963, **38**(12), 2834–2838, DOI: [10.1063/1.1733610](https://doi.org/10.1063/1.1733610).
- 77 J. D. L. Dutra, T. D. Bispo and R. O. Freire, LUMPAC Lanthanide Luminescence Software: Efficient and User Friendly, *J. Comput. Chem.*, 2014, **35**(10), 772–775, DOI: [10.1002/jcc.23542](https://doi.org/10.1002/jcc.23542).
- 78 H. Tan, Q. Li, C. Ma, Y. Song, F. Xu, S. Chen and L. Wang, Lanthanide Based Dual-Emission Fluorescent Probe for Detection of Mercury(II) in Milk, *Biosens. Bioelectron.*, 2015, **63**, 566–571, DOI: [10.1016/j.bios.2014.08.015](https://doi.org/10.1016/j.bios.2014.08.015).
- 79 M. A. Treto-Suárez, Y. Hidalgo-Rosa, E. Schott, X. Zarate and D. Páez-Hernández, Radiative Decay Channel Assessment to Understand the Sensing Mechanism of a Fluorescent Turn-on Al<sup>3+</sup> Chemosensor, *Int. J. Quantum Chem.*, 2020, **120**(3), 26083, DOI: [10.1002/qua.26083](https://doi.org/10.1002/qua.26083).

